Stellar and Solar Chromospheres and Attendant Phenomena

2

Thomas R. Ayres

University of Colorado, 389-UCB (CASA), Boulder, CO, United States

CHAPTER OUTLINE

1. INTRODUCTION

One might surmise that the physics of the stars and that of the Sun must be intimately connected. After all, physics is physics and the Sun is a star. However, any common ground fails at a granular level for the simple reason that sets the Sun apart from all the other stars: it is possible to observe the solar surface (and the interior, thanks to helioseismology) in remarkable detail with almost arbitrarily high temporal, spatial, and spectral resolution, free of interstellar absorption.

Furthermore, as a singular object of attention, the Sun has inspired long-term records of various phenomena such as the enigmatic sunspot cycle, for which detailed surface maps of the dark spots (initially drawings, more recently digital images) extend back four centuries or more. Meanwhile, the stars are so distant that observational limitations dictate more superficial examinations, certainly spatially unresolved, except in a few special cases. Also, the stars are so numerous and diverse

in size, mass, temperature, luminosity, chemical composition, age, etc., that statistical considerations must come into play. The wide but shallow view of the stars lends itself to equally superficial physical modeling. Thus, there is little to be learned about the fine details of solar phenomena from the necessarily more global examinations of the stars.

That said, studies of the stars can help our understanding of the Sun in a number of important ways. We have learned much from our privileged solar vantage point but still must appeal to the broader collection of sunlike stars to understand pivotal aspects of the solar condition. For example, is the Sun typical of G-type dwarfs? Or is the Sun special in some way that has allowed life to develop and flourish on one of its planets? What might the Sun have been like in its youth, when the solar system was still forming? Will normal evolutionary changes in our star someday threaten planetary habitability? Are there infrequent events on the Sun that might affect our technology-laden civilization right now, for which there is little or no historical experience because these episodes are rare? Observations of stars can help answer such questions. This is the playing field of the Solar-Stellar Connection laid out by Leo Goldberg a half-century ago in a prestigious Russell Lecture before the American Astronomical Society.

There is one more point to be made in favor of the stellar viewpoint: the necessarily macroscopic views of stars potentially can act as a filter to isolate important global phenomena that might be glossed over in the microscopic details of solar observations: a forest view despite the trees.

2. WHY CHROMOSPHERES EXIST

2.1 STELLAR CONVECTION ZONES

The chromosphere story begins with convection. The presence of an outer convective envelope is the main characteristic that distinguishes late-type (cool) stars from their early type (hot) cousins. Convection zones make their appearance at the early F spectral types, for which the effective temperature, T_{eff}, is about 7000K; increase in thickness through the solar spectral types (G2 V: $T_{eff} \approx 5770K$), down to the K-types ($T_{eff} \approx 4500K$); then into the cooler M's ($T_{eff} \approx 3500K$), which become fully convective by mid-M.

Convection plays several key roles in defining the physical state of the stellar outer atmosphere (sequentially outward from the stellar surface): *photosphere* (6500−4000K [at solar T_{eff}]), *chromosphere* (5000−8000K), *transition zone* (TZ) (10^4−10^5K), and *corona* $\left(T \gtrsim 10^6 \text{ K}\right)$:

1. Convective turbulence, and collapse of convective granules, together produce acoustic noise, which powers internal seismic waves and leaks into the chromosphere, inducing shocks and other dynamical effects.
2. Convection transforms the solid body rotation of a star into differential zonal flows (the Sun's equator rotates almost 40% faster than the poles). Differential rotation, in turn, has a central role in the (α-Ω) dynamo generation of strong

magnetic fields in the stellar interior, at the interface between the convective and radiative zones. The internal magnetic flux ropes occasionally become buoyant, rise through the convective envelope, then erupt into the surface layers as active regions, often showing a great deal of complexity. These dynamic magnetic ecosystems cause heating in the chromosphere, and transient events such as flares and coronal mass ejections.

3. Convective turbulence also can directly produce (by the α-α effect) small-scale magnetic fields in the near-surface layers, which can bubble up into the photosphere as ephemeral bipoles and other types of disorganized field.

4. Chaotic flows associated with the overturning convection cells kinematically buffet the photospheric footpoints of small-scale magnetic flux tubes, launching various types of Alfvén waves and magnetosonic disturbances that can dissipate heat higher up. Organized larger-scale horizontal convective flows can sweep up the small-scale field and collect it into discrete surface patterns called the supergranulation network. There, flux concentrations of opposite polarity are driven against one another by turbulence in the subduction lanes of the large-scale pattern. Reconnection heating can occur as a consequence, sometimes ejecting high-speed gas plumes.

Given the myriad roles of convection, it is unsurprising that solar-like high-energy activity is confined mainly to late-type stars.

2.2 THE SOLAR CHROMOSPHERE

Fig. 2.1 depicts a full-disk filtergram of the Sun taken in the Ca II 3933 Å K resonance line during a period of moderate solar activity. The K line brightens in magnetically disturbed areas where local chromospheric heating is elevated. The image illustrates several of the magnetic-related features mentioned earlier, specifically their chromospheric counterparts. Numerous sunspots, some organized in groups, appear as small, dark, roughly circular patches (dim in visible light; apparently also in chromospheric Ca II emission). Surrounding the dark spots are halos of bright Ca II plage. These are extensive, moderately magnetic areas (≈ 100 G, spatially averaged) initially associated with emerging sunspots, but often persist long after the magnetically intense spots (≈ 1000 G) have decayed. Further from the active regions are additional Ca II bright mottles organized in the lacy pattern of the supergranulation network. At a finer spatial scale, one also would see a peppering of Ca II bright points in the network cell interiors, which represent transient chromospheric excitation mainly by shock waves.

As illustrated in Fig. 2.2, Hα 6563 Å filtergrams have a significantly different appearance. This is partly because the formation of the subordinate hydrogen line has a more complex relationship to plasma properties owing to the difficulty of populating the 10 eV lower level of the transition and partly because, as the lightest element, hydrogen is the most affected by thermal Doppler broadening. The Hα feature can be seen in relative absorption or emission, depending on local physical conditions and also at what velocity displacement the line profile is sampled
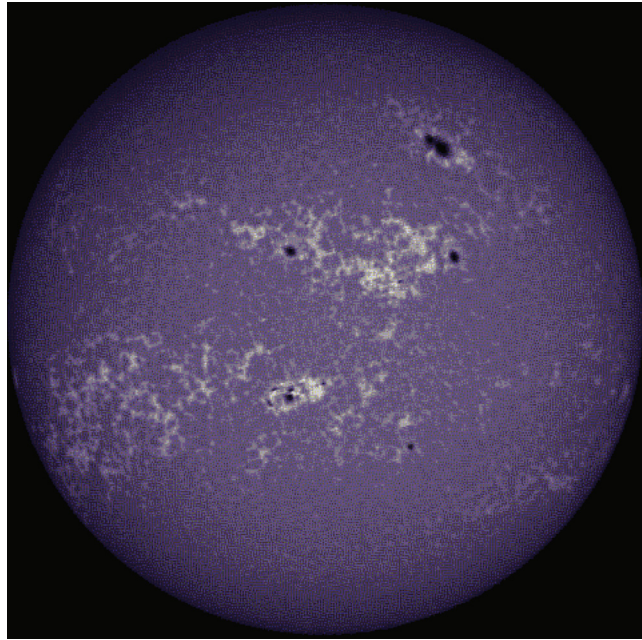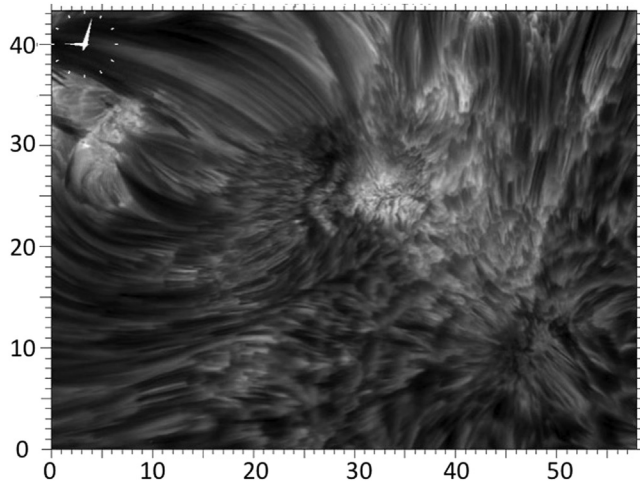
FIGURE 2.1

Ca II K-line (3933 Å) full-disk filtergram of solar chromosphere. Smaller dark areas are sunspot umbrae; surrounding lighter patches are chromospheric plage. Away from the spot groups, the brighter, lacy patterns are part of the supergranulation network. Not visible in this global image are small-scale transient Ca II bright points found in the internetwork regions.

From the Big Bear Solar Observatory.

(primarily owing to the Doppler broadening effect). Unlike Ca II images, which are dominated by collections of small-scale bright features near the lower-altitude foot-points of magnetic structures, the Hα pictures are composed of light and dark horizontal striations of various lengths, sometimes organized in radially spoked rosettes, all of which trace the higher altitude extensions of the magnetic field, forming the complex topology of the chromospheric canopy.

A common feature of full-disk Hα filtergrams are long, dark, narrow curvilinear features called filaments (prominences when seen in emission at the limb). These are unusually cool ($\approx 10^4$K) and dense plasma structures, in the otherwise hot ($\approx 10^6$K) tenuous corona, suspended high above the surface inside long-lived magnetic flux ropes.

In fact, prominence-like structures are inferred to exist on a few fast-rotating, active stars such as the K dwarf AB Doradus (Collier Cameron et al., 1990) and the G giant FK Comae Berenices (Huenemoerder et al., 1993). The signature is Doppler-shifted components in Hα that are synchronized with the rotation period,

FIGURE 2.2

High-resolution Hα (6563 Å) filtergram of solar chromosphere. Scales are in arcseconds.

From the Swedish Solar Observatory.

but whose projected velocities exceed that of the stellar surface by as much as a factor of two, which suggests a physical extension to perhaps a stellar radius above the photosphere. The fast rotation of the host stars makes high-altitude prominence-like structures especially easy to detect spectroscopically. Nevertheless, such coronal condensations probably are common among cool stars.

2.3 STELLAR CHROMOSPHERES

Like the solar counterpart, stellar chromospheres are known principally from optical emission lines, especially Ca II H and K and Hα (the latter usually is seen in absorption, although emission is common in more active stars). As shown in Fig. 2.3, the Ca II emission cores sit at the bottoms of broad, deep photospheric absorption features, which completely dominate the 3900-4000 Å wavelength interval in stars such as the Sun. In fact, thanks to favorable atomic physics, the Ca II resonance doublet is the strongest feature in the visible solar spectrum, even through calcium is not particularly abundant (compared with iron, for instance). In contrast, the most prominent hydrogen line in the visible, Hα, is much weaker, despite the overwhelming abundance of hydrogen, now owing to unfavorable atomic physics (the 10 eV lower level of Hα is only weakly populated in a cool atmosphere).

The chromospheric Ca II emission cores are doubly-reversed (M-shaped). They barely are discernible in low-activity G dwarfs such as the Sun but strengthen in active dwarfs (or solar plage regions). In late-type stars, the Ca II emission features broaden systematically with increasing absolute visual luminosity over a remarkable
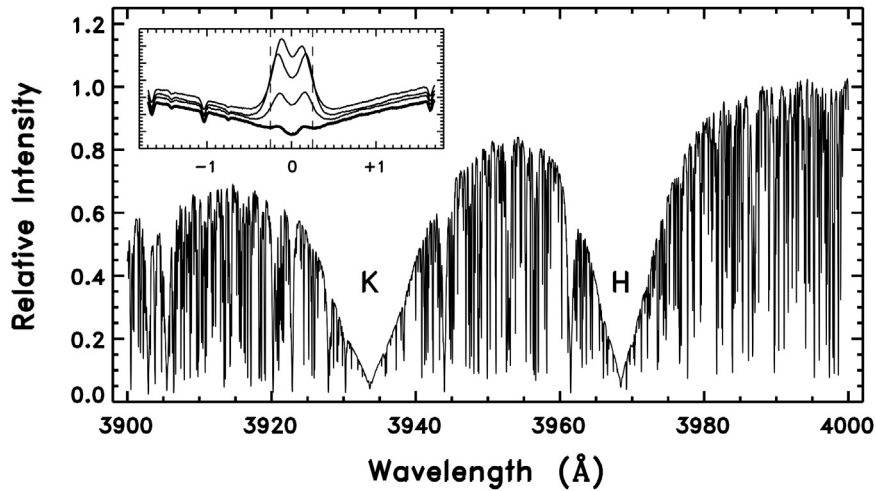
FIGURE 2.3

Ca II H and K lines in the solar spectrum, dominating the violet region. Inset shows blowup of K-line core in quiet Sun (lower, thicker curve) and three plage regions (thinner, higher curves): *x*-axis is wavelength displacement from line center in Å. Note that the full widths at half maximum (FWHM) (delimited by vertical dashed lines) are similar; the K_1 minimum features become broader with increasing activity (stronger K-line emission) but the K_2 peak separations become perhaps slightly narrower.

From the National Solar Observatory Fourier transform spectrometer archive.

15 stellar magnitudes. This is called the Wilson-Bappu effect (WBE), named after its codiscoverers (Wilson and Bappu, 1957); it is illustrated in Fig. 2.4.

2.4 WHY ARE CHROMOSPHERES SO THICK?

The chromospheric temperature inversion exists because nonradiative heating above the photosphere disrupts the classical radiative equilibrium (RE) stratification. A remarkable characteristic of chromospheres that begs explanation is why they are so thick. Semiempirical solar models (Vernazza et al., 1981) indicated that the layer is about 1500 km in extent, roughly 10 pressure scale heights, three times thicker than the photosphere. Empirical measurements, especially at total eclipses, have proposed even larger extents.

As we will see subsequently, this key structural property of the chromosphere can be addressed even without full knowledge of the possible heating mechanisms.

How Is the Chromosphere Cooled? The chromosphere is an ideal environment to explore the balance, or lack of balance, between heating and cooling processes. The reason is that although the heating mechanisms might be varied and complex, the cooling is straightforward: creation of photons by collisional interactions and then their escape from the chromosphere. This radiative cooling dominates in the
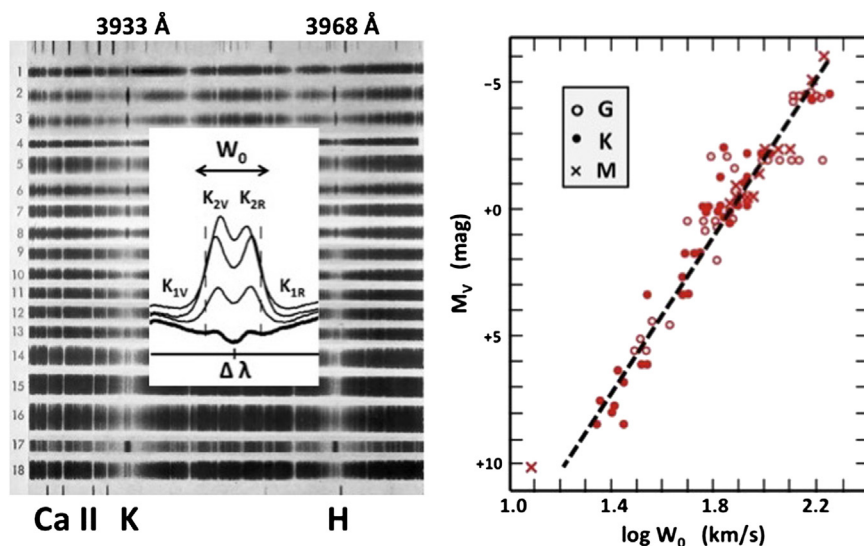
FIGURE 2.4

Left: stacked photographic spectra of 18 representative late-type stars (higher intensities are darker) in the Ca II region. Star 3 has narrow H and K emissions, whereas star 15 has noticeably broader, doubly reversed profiles (see schematic tracing of reversal shapes in inset). Right: stellar Wilson—Bappu effect: full width at half maximum intensity (W_0, expressed in equivalent velocity units) of the Ca II K-line emission core increases systematically with absolute visual magnitude.

*Adapted from Wilson, O.C., Bappu, V.M.K., 1957. Astrophys. J. **125**, 661.*

low-density layers because the gas is optically thin, so local convection is inhibited; while the temperature gradients are relatively mild, so heat conduction is suppressed (except at the steep TZ interface at the top of the chromosphere).

A lucky consequence of radiative cooling control is that, in principle, solar observers can record the escaping chromospheric radiation directly, so it is a simple matter conceptually to count all the radiative losses to determine the cooling, and thus also the incident heating. However, given the observational challenges to record often subtle chromospheric emissions across a wide range of species and wavelengths, a more practical way to carry out the radiative cooling inventory is to calculate the individual contributions using a chromospheric model, especially when it is "calibrated" against the more robust chromospheric signatures (Mg II and Ca II).

By this approach, Anderson and Athay (1989) estimated chromospheric radiative losses for the quiet Sun of 1.4×10^7 erg/cm^2 s. The authors found that Fe II was responsible for about half the total line cooling (Mg II and Ca II accounted for much of the rest), and that the energy dissipation was nearly constant across the chromospheric temperature plateau, 6000—8000K.

The chromospheric energy loss is only about 0.02% of the solar bolometric surface flux, $\mathcal{F}_{\text{bol}}^{\odot} = 6 \times 10^{10}$ erg/cm^2 s. The corresponding fractions for the TZ and corona are down by additional orders of magnitude. In this light, the outer atmospheric heating might seem trivial. Nevertheless, one must keep in mind that it is source of the Sun's high-energy activity that feeds Earth-affecting space weather.

Chromospheric Structure. In the early-1960s, Thomas and Athay (1961) argued that the chromospheric temperature rise resulted in part from a shift in the radiative cooling from the negative hydrogen ion, H$^-$ (dominant visible and near-infrared [IR] broadband opacity) to hydrogen bound-bound transitions (Lyα, Hα) and bound-free continua (Balmer and Paschen), which can be excited at higher temperatures than H$^-$.

In the late-1970s, T. Ayres (1979) pointed out that the H$^-$ continuum cooling and that of important chromospheric resonance lines all are similar in magnitude and all have the same dependence on the electron density. So, it might be that the electron density itself was the key to understanding the chromospheric temperature inversion. In fact, solar and stellar semiempirical models available at the time almost invariably had remarkably constant electron densities [$n_e(\text{cm}^{-3})$] in the chromospheric layers despite the typical factor of 10^4 exponential decline of the hydrogen density [protons + neutrals: $n_H(\text{cm}^{-3})$] over the same height range.

The Ionization Valve Effect. A simple analytical framework was proposed by Ayres (1979) to understand the basic foundations of chromospheric structure. The underlying mechanism later was called the ionization valve effect. Here is how it works.

Photospheric temperatures of a cool star decrease monotonically outward in RE, eventually stabilizing at a boundary value ($T \approx 0.8\,T_{\text{eff}} \approx 4850$K for the Sun) in the optically thin layers. At these temperatures, hydrogen is almost completely neutral, but a soft lower boundary on the ionization fraction, $n_e/n_H \approx 10^{-4}$, is maintained by the easily ionized metals (such as iron). The atmosphere can remain in balance at these low temperatures because both the radiative heating and cooling are controlled by mirror-image processes in the same species (H$^-$).

However, if there is extra, *nonradiative* energy deposition (e.g., acoustic shocks, magnetosonic waves, magnetic reconnection, and so forth) in these high layers, the gas cannot rid itself of the additional heat in its baseline low ionization state. The reason is that the radiative cooling (per gram of material) is proportional to the electron density, and thus must follow the precipitous outward hydrostatic decline of the hydrogen density (because at low temperatures, $n_e \approx 10^{-4}\,n_H$). Given the outwardly falling radiative cooling, any increased energy input will cause a thermal instability, forcing the temperatures to rise above the RE boundary value, until enhanced ionization boosts the collisionally induced thermal emission. This tipping point defines the initial chromospheric temperature rise.

Above that point, increasing ionization can keep up with a more or less height-independent extra heating over many pressure scale heights, even despite the rapid outward decline of n_H, because when hydrogen begins to ionize ($T > 5000$K), there are lots of electrons available (i.e., n_e/n_H can increase *four orders of magnitude* from

the metal-dominated limit 10^{-4} at and below about 4500K; up to ~ 1 near 8000K, where hydrogen is fully stripped). This region of slowly rising temperatures but rapidly increasing ionization is the middle chromosphere.

Once the hydrogen is almost completely ionized, however, the gas has run out of new cooling electrons and no longer can compensate for extra heating by slowly increasing the temperatures outward. Rather, a catastrophic thermal instability must ensue, imposing a sharp temperature rise ($10^4 \rightarrow 10^6$ K) at the top of the thick, nearly isothermal (6000−8000K), middle chromosphere. This second inversion is the chromosphere-corona TZ.

Now, let us consider the scenario more quantitatively, piece by piece.

Low-Temperature Metal Ionization. Near the top of the photosphere ($T < 5000$K), hydrogen is essentially neutral (owing to its high 13.6 eV ionization potential) and electrons come mainly from the big-three easily ionized metals: Mg, Si, and Fe, each about 3.5×10^{-5} by number relative to hydrogen. Between 3000 and 5000K, the ionization fractions of these species are close to unity, so: $n_e \approx (A_{Mg} + A_{Si} + A_{Fe})n_H \approx 1.2 \times 10^{-4}\widetilde{A}\; n_H$, where the *A's* are abundances relative to hydrogen, and $\widetilde{A}$ is a relative metallicity factor introduced for the general stellar case $\left(\widetilde{A}_\odot \equiv 1\right)$.

H^- Cooling and Heating. In a normal late-type atmosphere, the broadband visible and near-IR opacity (i.e., that which controls the bolometric flow of radiative energy through the photosphere) is dominated by the loosely bound (0.75 eV) negative hydrogen ion, H^-. Under such conditions, in the Sun, temperatures fall steadily outward from about 6500K in the deep photosphere $(\tau_{H^-} \approx 1)$ until they reach a boundary value of about 4850K roughly 500 km above $\tau_{H^-} \approx 1$. (The continuum optical depth unity surface could be called the *see level*, the deepest layers visible to an external observer.)

H^- cools the gas by associative attachment (analogous to recombination for ions): a free electron interacts with the polarization electric field of a neutral hydrogen atom and can be captured into the single weakly bound state of the quasimolecule. The kinetic energy of the captured electron plus the binding energy, 0.75 eV, is liberated as a photon (with wavelength, $\lambda \lesssim 1.6\ \mu$). The packet of energy carried away by the photon represents a net drain from the local "thermal pool," i.e., cooling.

Radiative heating mainly is by the complementary process, photodetachment of H^-: a sufficiently energetic photon (below the dissociation limit at $1.6\ \mu$) ejects the loosely bound electron. The freed hot electron then thermalizes its energy by collisions with other particles in the gas, thereby heating the plasma.

In the solar outer photosphere, near the radiative boundary temperature (4850K), the H^- heating and cooling are in balance. On either side of the equilibrium temperature, the *net* heating (or cooling) scales as $\Delta T/T$ relative to the (large) absolute H^- cooling. Consequently, the *net* H^- cooling is significantly reduced near the boundary temperature, but on the other hand, the substantial H^- heating term is largely canceled.

Radiative Cooling by Lines. The most significant chromospheric cooling lines are Mg II h and k at 2800 Å, Ca II H and K at 3950 Å, and a series of strong transitions of singly ionized iron, mainly in the 2400-2600 Å interval. Of secondary importance are H I 1215 Å Lyα (primarily at the top of the chromosphere), Hα, and the Ca II subordinate IR triplet (near 8500 Å).

All of the parent species are the dominant ionization stages of the respective elements under chromospheric conditions. Mg II and Ca II have low-lying excited levels easily populated by collisions and connected to the ground state by pairs of strong near-UV resonance transitions. Mg II is more important than Ca II because magnesium is 15 times more abundant. Fe II has generally weaker resonance transitions than Mg II, but more of them; and like Mg II, is important owing to the large abundance of iron.

The resonance line cooling works differently from the H$^-$ associative attachment described earlier, but follows the same principle: a collisional interaction creates a photon, which then escapes from the region, carrying away the energy of formation. In this case, the interaction is an inelastic collision between a fast free electron and the ion, which promotes one of the bound electrons into a higher orbital at the expense of most of the kinetic energy of the incident electron. Electrons are the dominant colliding partners, because the light particles have faster thermal speeds than the heavier hydrogen atoms and thus higher collision frequencies.

Resonance transitions such as Ca II H and K are characterized by very fast spontaneous radiative decays (Einstein A-values typically of order 10^8 s^{-1}). Consequently, an initial inelastic collisional excitation usually is followed by a spontaneous decay, producing a photon. If the newly minted photon travels a long distance, the energy it carries away would represent a net drain locally, thus cooling.

However, the most common situation at low densities is scattering: a resonance transition initially is *photo*-excited and then almost immediately decays radiatively. The new photon is essentially identical to that absorbed in all respects (except perhaps the direction of flight). The main way in which a scattered photon is destroyed is when the radiative decay that normally follows the photo-excitation is short-circuited by an inelastic collisional de-excitation.

When the collisional-deactivation rates are slow, as at low density, an absorbed photon is less likely to be removed from the radiation field after each photo-excitation, and thus ultimately might escape the atmosphere after a long journey of many scatterings. On the other hand, when deactivation rates are fast, as at high density, an absorbed photon more likely would be thermalized by a downward collision after each photo-excitation. In the high-collision-rate limit, photons are able to travel only a single optical depth, on average, before being destroyed.

The multiple scattering process is characterized by a thermalization depth, Λ, the average number of vertical line-center optical depths a newly created photon can traverse before destruction. When collision rates are high, $\Lambda \approx 1$. However, when collision rates are low, Λ could be very large, thousands or many thousands of optical depths for chromospheric resonance lines.

Several aspects of the scattering process control Λ, especially frequency redistributions. This effect causes photons to random-walk not only in physical space but also diffuse through the line profile in frequency. This diffusion is important because photons escape more readily in the transparent line wings than in the opaque line core. Such nuances make the calculation of thermalization depths and associated escape probabilities tricky.

Regardless, resonance lines of abundant species are capable of removing collisionally-created photons efficiently from deep in the chromosphere, and thus can be potent radiative coolants. When a species is emitting within a thermalization depth of the surface, we call the transition effectively optically thin, or simply effectively thin.

The collision-induced radiative cooling can be expressed as a differential increment to the local energy flux, $\mathcal{F}$, with respect to height. For our purposes, the most convenient height scale is the mass column density $m(\mathrm{g/cm^2})$, the mass of gas in a $\mathrm{cm^2}$ column above a given altitude. In the solar atmosphere, m decreases two orders of magnitude from 4 g/cm^2 at $\tau_{\mathrm{H^-}} \approx 1$ to 0.03 g/cm^2 at $\tau_{\mathrm{H^-}} \approx 10^{-4}$ (top of the photosphere); then another four orders of magnitude through the chromosphere itself. In these variables, the line cooling can be written as $d\mathcal{F}_\ell^{\mathrm{cooling}}/dm$.

For strong resonance lines under chromospheric conditions, the radiative cooling is directly proportional to the upward collisional rate because virtually every excitation results in emission of a photon; but with a correction for the fraction able to escape the region: $\frac{d\mathcal{F}_\ell^{\mathrm{cooling}}}{dm} \approx w\frac{n_l C_{lu}}{\rho}\left(\frac{hc}{\lambda_{lu}}\right) \mathrm{erg/s\ g}$, where n_l is the population of the lower level; C_{lu} is the upward collision rate; λ_{lu} is the transition wavelength (parenthetical term is the photon energy); w is a cooling escape fraction that accounts for the collisionally created photons that actually cool the gas; and ρ is the matter density (g/cm^3). The latter factor converts the expression from physical height, z, to mass column density, m (because $dm = \rho\,dz$). (A useful relation for later: $\rho \approx 1.4\,m_H\,n_H$ for a 10% helium abundance by number; m_H is the mass of the hydrogen atom.)

If the species is the dominant ionization stage of the element, and most of the population resides in the ground state (normally the case), then: $n_l \approx A_{el}\,n_H$, where A_{el} is the abundance of the element by number relative to hydrogen.

In the effectively thin layers, the minimum value of w likely is $\approx\frac{1}{2}$, representing the photons scattering in the outward hemisphere, which ultimately escape the atmosphere. Note that $w \to 0$ in the effectively thick limit, where all the photons are thermalized more or less locally.

The collision rate can be written as $C_{lu} = n_e \Omega_{lu}(T/5000)^{-1/2}e^{-hc/\lambda kT}$ s^{-1}. Here, Ω_{lu} is the collision strength, which can be evaluated as $\gamma_{lu}(T)/\left(g_l\sqrt{5000}\right)$, where $\gamma_{lu}(T)$ is the factor tabulated in, for example, the Chianti Atomic Database, and g_l is the statistical weight of the lower level. For ions, $\gamma_{lu}(T)$ has a slow logarithmic dependence on temperature (Burgess and Tully, 1992).

Mg II h and k provide a significant fraction of the total resonance line cooling in the solar chromosphere, perhaps as much as 30%, so are a useful bellwether for the total effect. Substituting parameters appropriate for these lines from *Chianti* into the previous equations, and taking $w \approx 1/2$, yields:

$$\frac{d\mathcal{F}_{\text{Mg II}}^{\text{cooling}}}{dm} \approx \left[6.3 \times 10^{+1} (T/5000)^{-1/2} e^{-51390/T} \right] \widetilde{A} n_e \text{ erg/s g} \approx 2.2 \times 10^{-3} \widetilde{A} n_e$$
$$(T = 5000 \text{K}).$$

Here, the magnesium abundance was assumed to scale as the stellar metallicity. A similar calculation for Ca II H and K yields a coefficient of 1.5×10^{-3} (5000K).

Important Fe II is more complicated, given its numerous strong UV transitions. An estimate can be obtained by considering the ground state and four lowest excited levels, and the associated resonance transitions to higher levels. Assuming pure-collisional population ratios and the *Chianti* collision strengths yields a numerical factor of 3.6×10^{-3} (5000K), comparable to Mg II + Ca II (i.e., Fe II accounts for about half the resonance line total, as concluded by Anderson and Athay (1989) from their numerical modeling).

Instabilities and Stabilities. When nonradiative heating is present at the top of the photosphere, there should be a point (call it m_*), where the extra heating begins to overwhelm the ability of the gas to cool itself at low temperature. At that tipping point, the temperatures must break upward from the boundary value because of the mismatch between heating and cooling. Beyond the initial inversion, the radiative cooling can tap into the ionization valve to maintain quasistability with only slowly increasing temperatures, independent of the outward decline in the hydrogen density, until all the bound electrons are exhausted. A one-dimensional semiempirical reference model of the solar chromosphere in Fig. 2.5 illustrates some of these basic structural features.

In the middle photosphere, where the metal resonance lines are effectively thick and thus poor coolants, the H^- *net* cooling $(\sim (\Delta T/T) n_e)$ still can balance a significant nonradiative heat input with only a small ΔT as long as the hydrogen density is high enough (noting again that $n_e \approx 10^{-4} n_H$). Thus, there could be, and probably is, substantial nonradiative heating in the dense middle photosphere, which nevertheless might not be obvious because the temperature profile still could be close to that expected in RE (Ayres, 1975). However, as the hydrogen density continues to fall outward, and so too the radiative cooling, there will come a point at which H^- no longer can keep up with extra heating at small ΔT (and low ionization).

Generic Nonradiative Heating Rate. Because the radiative cooling is proportional to n_e, regardless of whether H^- or lines dominate, and the collective cooling must balance the nonradiative input, the constancy of the electron density in
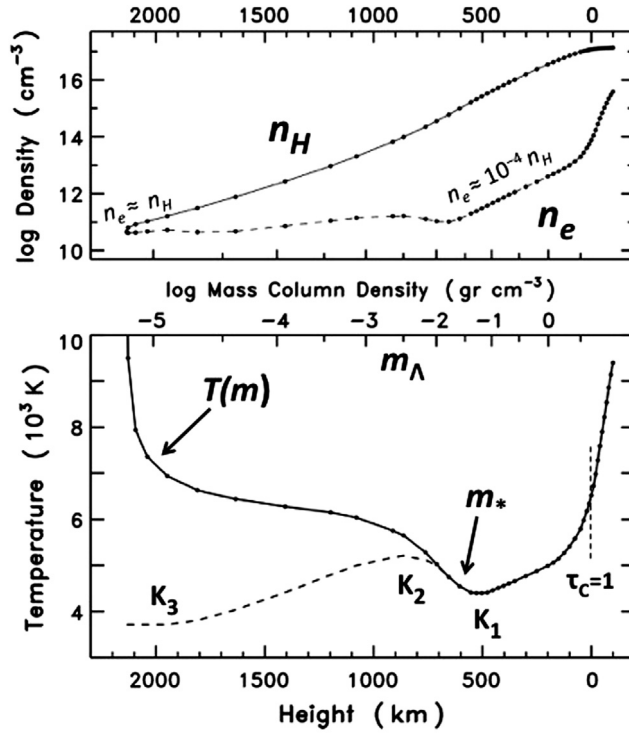
FIGURE 2.5

Lower panel: VAL-C' quiet Sun reference model of Maltby et al. (1986). Thick, warm chromospheric layer, above T_{min} region at top of photosphere, is terminated at left by steep rise to million-degree corona, through narrow transition zone. Critical mass column density, m_*, described in the text, is located just above T_{min}. Height zero is continuum optical depth unity at 5000 Å (the "see level"). Dashed curve represents the scattering source function (in equivalent temperatures) for the Ca II K line. The source function breaks downward from the temperature profile above T_{min} as Ca II photons begin to escape from the open boundary. m_Λ marked on the upper mass column density scale indicates the thermalization depth mentioned in the text. Different intensity features in the Ca II profile (Fig. 2.4: K_1, K_2, and K_3) are mappings of corresponding features in the source function, as indicated. Upper panel: Hydrogen and electron densities for the model, showing almost constant n_e in the chromosphere, as well as the $n_e \approx 10^{-4} n_H$ behavior in the photosphere where hydrogen is neutral and the electrons come from singly ionized metals.

semiempirical models suggests that the extra heating (per gram) is relatively constant with altitude above the base of the chromosphere (here designated m_*), as noted by Anderson and Athay (1989) from their model simulations.

With this assumption, the heating rate at m_* (or indeed anywhere in the chromosphere) can be estimated as $\frac{d\mathcal{F}^{\text{heating}}}{dm} = \text{const} = \mathcal{F}_{\text{tot}}m_*^{-1}$ erg/s g, where $\mathcal{F}_{\text{tot}}$ is the *total* extra heat deposited in the chromosphere ($\approx 1.4 \times 10^7$ erg/cm^2 s for the quiet Sun, as mentioned earlier).

We could generalize this expression to other stars if we knew how the total heating varied with surface gravity, effective temperature, and activity level. We can estimate these trends by considering the chromospheric fluxes of different types of stars (noting again that the radiative emissions are proxies for the nonradiative heating).

Bolometrically Normalized Fluxes. A useful way to compare chromospheric emission levels of different stars is to divide a cooling line flux, say $f_{\text{Mg II}}$, by the bolometric flux (total over all wavelengths) f_{bol} (both quantities in erg/cm^2 s at Earth). The stellar bolometric flux can be calculated from a formula based on, say, the Johnson visual *V*-band, with a bolometric correction that depends mainly on the stellar effective temperature.

The $f_{\text{Mg II}}/f_{\text{bol}}$ index tells us what fraction of the total stellar energy budget has been diverted to produce the chromospheric Mg II emission, at least the part that escapes to be detected remotely, so it is something like an efficiency factor (and typically small, $\approx \textit{few} \times 10^{-5}$). The $f_{\text{Mg II}}/f_{\text{bol}}$ ratio has the great virtue that it is independent of stellar sizes and distances, and thus is less biased in comparisons of different types of stars, such as dwarfs and giants. The $f_{\text{Mg II}}/f_{\text{bol}}$ ratio is equivalent to $L_{\text{Mg II}}/L_{\text{bol}}$ (and often written that way). Another useful equivalence is $\mathcal{F}_{\text{Mg II}}/\sigma T_{\text{eff}}^4$, where $\mathcal{F}$ is the surface flux (erg/cm^2 s at the star).

Stellar Mg II Emission Trends. We now consider the Mg II emissions of stars to gain insight into how the total chromospheric heating, $\mathcal{F}_{\text{tot}}$, might vary with stellar parameters. Mg II is superior to Ca II (or Fe II) for this purpose, because the near-UV Mg II core emissions show larger intensity contrasts than the often barely visible Ca II (or Fe II) reversals.

A valuable stellar Mg II inventory was provided by the venerable International Ultraviolet Explorer satellite (1978−96). These measurements can be summarized as follows:

1. At any given spectral type, there is a wide range of $L_{\text{Mg II}}/L_{\text{bol}}$ ratios extending upward from a soft lower limit, often called the basal flux.
2. The spread of $L_{\text{Mg II}}/L_{\text{bol}}$ values above the basal limit appears to be controlled by a hidden property of stars, which we might call their activeness (presumably related to elevated magnetic activity).
3. Mg II time series of individual stars show variability at the rotation period and also on longer time scales associated with stellar analogs of the decadal sunspot cycle. Nevertheless, the variability amplitude generally is much smaller than the $L_{\text{Mg II}}/L_{\text{bol}}$ spread between inactive and active stars.
4. The basal flux boundary, albeit fuzzy, displays a modest decline with decreasing effective temperature, something like $\mathcal{F}_{\text{Mg II}}/\sigma T_{\text{eff}}^4 \sim T_{\text{eff}}^{+2 \pm 2}$ (Linsky and Ayres, 1978).

The item 4 dependence implies $\mathcal{F}_{\text{Mg II}} \sim T_{\text{eff}}^{+6 \pm 2}$ along the basal flux trend. In other words, the baseline Mg II chromospheric surface flux, powered by some combination of acoustic shocks and the supergranulation network, falls off strongly with decreasing stellar effective temperature, perhaps even a little faster than expected from a strict proportionality with the bolometric surface flux.

Given the empirical Mg II trend, and the absolute chromospheric cooling for the quiet Sun, the total inferred stellar heating can be estimated as: $\mathcal{F}_{\text{tot}} \sim 1.4 \times 10^7 \ \widetilde{\mathcal{F}} \ \widetilde{T}_{\text{eff}}^{+6 \pm 2}$ erg/cm^2 s, where $\widetilde{T}_{\text{eff}}$ is the stellar effective temperature in solar units ($T_{\text{eff}}^{\odot} = 5770$K), and $\widetilde{\mathcal{F}}$ is an activeness factor to account for deviations from the basal heating law. For example, $\widetilde{\mathcal{F}} \approx 1$ for a low-activity star such as the Sun, whereas $\widetilde{\mathcal{F}} \approx 10$ for a solar plage region, or a young, active G dwarf. The (depth-independent) heating rate now can be written as: $\frac{d\mathcal{F}^{\text{heating}}}{dm} \approx 1.4 \times 10^7 \widetilde{\mathcal{F}} \widetilde{T}_{\text{eff}}^{+6 \pm 2} m_*^{-1}$.

Thickness of the Chromosphere. In equilibrium, the local cooling must balance the local heating (radiative plus nonradiative) throughout the chromosphere, in particular at the base, where temperatures are low enough that metal-dominated ionization still holds. For the sake of argument, suppose that the radiative cooling at m_*, evaluated at a chromospheric base temperature of ≈ 5000K, is the Fe II plus Ca II effectively thin result (Mg II is the most likely of the three to be effectively thick). This acknowledges that the H$^-$ cooling essentially cancels the photospheric radiative heating at that temperature, so we can safely ignore both contributions in the energy equation. The Fe II + Ca II cooling rate is $\frac{d\mathcal{F}_{\text{tot}}^{\text{cooling}}}{dm}(m_*) \approx 5.1 \times 10^{-3} \widetilde{A} \, n_e^*$ erg/s g (5000K). The leading numerical factor shows only a mild increase over the range 5000−8000K, so the metal cooling per gram depends mainly on the electron density.

At low temperatures, as described earlier, the electron density is proportional to the total hydrogen density, n_H. The latter, in turn, is related to the mass column density, m, through the hydrostatic equilibrium condition: g $m = 1.1 \, n_H k \, T$, where g is the stellar surface gravity (g$_\odot = 2.74 \times 10^4$ cm/s^2) and k is Boltzmann's constant. The left-hand side represents the weight of the mass column and the right-hand side is the gas pressure at the base of the column. The latter invokes the perfect gas law, a 10% helium abundance by number, and negligible ionization. Solving for the hydrogen density, introducing the result into the metal-ionization, then substituting for n_e^* in the cooling function yields: $\frac{d\mathcal{F}^{\text{cooling}}}{dm}(m_*) \approx 2.2 \times 10^{10} \widetilde{A}^2 \ \widetilde{g} m_*$ erg/s g, where $\widetilde{g} = g_*/g_\odot$ accounts for nonsolar surface gravities. Here, the metallicity factor enters squared: one power for the line cooling and the other for the low-temperature metal ionization. Equating the heating and cooling expressions at the tipping point yields: $m_* \approx 0.025 \widetilde{A}^{-1} \widetilde{\mathcal{F}}^{+\frac{1}{2}} \widetilde{g}^{-\frac{1}{2}} \widetilde{T}_{\text{eff}}^{+3 \pm 1}$ g/cm^2. Note that the chromospheric thickness goes as the inverse square-root of the key structural parameter, surface gravity. In other words, a lower-gravity atmosphere, with its lower densities,

must push the chromospheric inversion inward in mass column density to reach a depth where there are enough electrons to fuel the metal-ionization dominated cooling. Together with the other dependencies, the relation says that chromospheres become thicker in lower gravity stars (e.g., giants), metal-poor objects, more active stars, and with increasing effective temperature.

In the semiempirical quiet Sun model VAL-C′ of Maltby et al. (1986), the column mass density at the base and initial rise of the chromosphere is about $0.01-0.05$ g/cm^2 (for the height range $710-530$ km [$5000-4400$K]). The modelized location of the solar inversion agrees reasonably well with the numerical coefficient in the m_* scaling law, which is encouraging.

Mean Electron Density of the Chromosphere. Substituting the m_* relation into the expression for n_H, then that result into the low-temperature metal ionization (again for $T \approx 5000$K) yields a second scaling law: $n_e^* \sim 1.1 \times 10^{11} \widetilde{\mathcal{F}}^{+\frac{1}{2}} \widetilde{g}^{+\frac{1}{2}} \widetilde{T}_{\mathrm{eff}}^{+3\pm 1}$ cm^{-3}. Note that the metallicity factor has canceled out. This relation says that a thin chromosphere (small m_*, typically high g) must have a larger mean electron density to radiate away the same total extra heat input as a thick chromosphere (large m_*, typically low g). In addition, the mean electron density rises with increasing activeness. However, both n_e^* and m_* depend on the activeness factor in the same way: a more active atmosphere is thicker *and* has a higher electron density.

Curiously, m_* depends strongly on metallicity (inversely), whereas n_e^* does not at all, at least when metal ions dominate the radiative cooling. This says that a metal-poor chromosphere will be thicker but will have the *same* mean electron density compared with a solar-abundance chromosphere of the same gravity and activity.

The numerical coefficient compares well with the $n_e \approx 1.0 - 1.7 \times 10^{11}$ cm^{-3} found above the $T_{\min}$ in the VAL-C′ model (1.1×10^{11} at 5000K). Also, the model C′ electron density is relatively constant in the chromospheric layers, whereas the hydrogen density falls outward about four orders of magnitude (see Fig. 2.5). The near-constancy of n_e over the same height range where n_H is dropping precipitously supports the basic premise of the ionization valve effect: It is all about the electrons.

A semiempirical chromospheric model for the red giant star Aldebaran (α Tauri: K5 III; $T_{\mathrm{eff}} = 3920$K, log g = 1.25, solar metallicity), published by McMurry (1999), has log $m_* = -0.5$ g/cm^2 and a chromospheric electron density of $1 - 10 \times 10^8$ cm^{-3}, with an average of about 8×10^8 cm^{-3} in the hotter layers ($6000-8000$K). Over the same range in mass column, the hydrogen density drops the familiar four orders of magnitude. For these stellar parameters, the scaling laws predict log $m_* = -0.5$ g/cm^2 and $n_e^* = 9 \times 10^8$ cm^{-3}; again, not bad agreement.

An older model chromosphere for the metal-deficient red giant Arcturus (α Boötis; K1 III; $T_{\mathrm{eff}} \approx 4250$K; log g ≈ 1.7; log $\widetilde{A} \approx -0.5$), published by Ayres and Linsky (1975), has log $m \approx +0.25$ and an electron density of $0.5 - 1.7 \times 10^9$ ($5000-8000$K). For the given stellar parameters, the scaling laws predict: log $m \approx -0.15$ and $n_e^* = 1.9 \times 10^9$. Compared with the roughly similar

red giant α Tau, aside from metallicity, the α Boo chromosphere is thicker but has about the same electron density. Again, the agreement with the scaling laws is encouraging.

2.5 THE WILSON−BAPPU EFFECT

An indirect way to test the chromospheric scaling laws is to assess their impact on the WBE mentioned earlier. Observations suggest $W_0 \sim \widetilde{A}^{\alpha} \widetilde{\mathcal{F}}^{\beta} \widetilde{g}^{\gamma} \widetilde{T}_{\text{eff}}^{\delta}$, where W_0 is the FWHM of the Ca II K (or Mg II k) emission core. Consensus empirical values for the power law indices are: $\alpha \approx 0$, $\beta \approx 0$, $-0.23 \leq \gamma \leq -0.20$, and $1.3 \leq \delta \leq 1.7$ (Linsky, 1999).

The emission width thus displays, remarkably, almost no sensitivity to metallicity or activeness. The dependence on effective temperature is mild, noting that T_{eff} varies only a factor of two from cool M-types to the warm F-types. The main sensitivity is the inverse dependence on surface gravity, because g decreases three or four orders of magnitude from dwarfs to supergiants. Despite the weak sensitivity of W_0 to activeness, Ca II (and Mg II) profiles of solar plage and active G dwarfs reveal that the *base* of the emission profile *broadens* with increasing $\widetilde{\mathcal{F}}$, whereas, counterintuitively, the separation of the peaks at the *top* of the profile seems to *narrow*, leaving the FWHM more or less unchanged (Ayres, 1979).

Now, we make a crucial assumption: the edges of the emission core just inside the K_1 minimum features are controlled by the Lorentzian wings of the line profile. In the wings, the opacity depends quadratically on the wavelength shift, $\Delta\lambda$, from line center: $\phi(\Delta\lambda) \sim \Delta\lambda^{-2}$. In the central Doppler core, on the other hand, the dependence is exponential, $\phi(\Delta\lambda) \sim e^{-\Delta\lambda^2/\Delta\lambda_D^2}$ (here, $\Delta\lambda_D$ is the Doppler width, related to local thermal and turbulent velocities).

The Lorentzian assumption is contrary to early attempts to understand the WBE, which assumed that the emission features form in the Doppler core; consequently, the width would be dictated by chromospheric velocity fields (e.g., Hoyle and Wilson, 1958). This is a reasonable expectation in principle, but in practice the implied velocities (already near-sonic in the Sun) would quickly become supersonic in giants and supergiants (e.g., Fig. 2.4, noting that the chromospheric sound speed is only about 7 km/s). Such extreme dynamics would be difficult to sustain in the face of strong dissipation by shocks. In that respect, Lorentzian control of the outer profile seems physically more appealing.

To proceed further, we can apply one of the Eddington−Barbier relations, based on analytical solutions of the radiation transport equation. It says that at a given wavelength in the line profile, $\phi(\Delta\lambda)$, one can "see" down to the atmospheric depths (and their associated thermal emission) corresponding to $\tau \approx 1$ *at that wavelength*. Thus, as one tunes through the line profile from the transparent far wings inward to the opaque core, the optical depth unity surface sweeps upward through the atmosphere, encountering progressively lower temperature layers and thus lower intensities, ultimately passing through the chromospheric temperature inversion, which then maps onto the profile as the initial $K_1 \rightarrow K_2$ emission rise.

Making these assumptions, it is easy to show that $\Delta\lambda_{K_1} \sim A_{Ca}^{+\frac{1}{2}} m_*^{+\frac{1}{2}}$. In other words, as the chromosphere thickens, the base of the emission reversal moves further from line center. The specific square root relationship works only for species, such as Ca II and Mg II, that are the dominant ionization stages at chromospheric temperatures. Then, the column density of (ground-state) absorbers is directly proportional to the column density of hydrogen, $N_H(\text{cm}^{-2})$, and thus also the mass column ($m \approx 1.4\, m_H N_H$).

Substituting the scaling law for m_* yields: $\Delta\lambda_{K_1} \sim \widetilde{\mathcal{F}}^{+\frac{1}{4}} \widetilde{g}^{-\frac{1}{4}} \widetilde{T}_{\text{eff}}^{+\frac{3}{2} \pm \frac{1}{2}}$, assuming that the calcium abundance follows the metallicity, $\widetilde{A}$, which then cancels that factor in m_*. This relation shows a similar mild inverse dependence on surface gravity as the consensus index for W_0, a weak sensitivity to activeness, no dependence on metallicity, and a positive moderate dependence on effective temperature.

A similar scaling relation can be worked out for the separation of the K_2 emission peaks. The formulation is more complicated because the scattering thermalization depth, Λ, mentioned earlier, comes into play. The key is that the latter tends to scale inversely as the electron density, $\Lambda \sim n_e^{-1}$. This has a significant impact on the $\Delta\lambda_{K_2}$ relation, which turns out to be $\widetilde{\mathcal{F}}^{-\frac{1}{4}} \widetilde{g}^{-\frac{1}{4}} \widetilde{T}_{\text{eff}}^{-\frac{3}{2} \pm \frac{1}{2}} \xi^{+\frac{1}{2}}$, where the new quantity ξ is a typical Doppler velocity in the upper chromosphere.

Note that $\Delta\lambda_{K_2}$ has the *same* dependence on surface gravity as $\Delta\lambda_{K_1}$ and likewise none on metallicity, but *opposite* sensitivities to the other two parameters, especially activeness. This says that $\Delta\lambda_{K2}$ also widens with decreasing surface gravity, like $\Delta\lambda_{K_1}$, but *narrows* with *increasing activity*, contrary to $\Delta\lambda_{K_1}$. This matches the counterintuitive behavior seen in plage profiles of Ca II.

Because the WBE width falls roughly midway between $\Delta\lambda_{K_1}$ and $\Delta\lambda_{K_2}$, the contrary behavior with respect to $\widetilde{\mathcal{F}}$ and $\widetilde{T}_{\text{eff}}$ suggests that W_0 will be less sensitive to these parameters, with exponents intermediate, perhaps even close to zero (as is the case for $\widetilde{\mathcal{F}}$ empirically). Also, because $\Delta\lambda_{K_1}$ and $\Delta\lambda_{K_2}$ display no sensitivity to metallicity, it stands to reason that the WBE width would not either, as observed.

In short, despite the enormous simplifications of the analytical arguments, the remarkable agreement of the scaling law predictions with the general properties of the WBE supports the idea that chromospheres owe their peculiar properties, especially their great thickness, mainly to the ionization valve effect rather than, say, to the specific heating mechanism(s) or the particular cooling opacities.

It used to be thought that the WBE was caused by a dramatic increase in atmospheric turbulence, going from dwarfs to giants, which would greatly enhance the Doppler broadening of the Ca II cores in the luminous stars. Now, we have seen an alternative view in which the Ca II width is controlled by the thickness of the chromosphere, which in turn adjusts itself to the impact of nonradiative heating according to a pressure-dependent instability in the low-temperature cooling. In this sense, the WBE is a *barometer*, not a *tachometer*.

## 3. THE ROTATION—AGE—ACTIVITY CONNECTION
3.1 BACKGROUND

About 50 years ago (a year before Goldberg's pivotal lecture on the solar—stellar connection), A. Skumanich, a noted solar physicist at the High Altitude Observatory in Boulder, Colorado, published a letter in the *Astrophysical Journal* announcing the discovery of a rotation—age—activity connection among late-type dwarf stars of solar type. This remarkable note, a scant two-plus pages in length, became one of the most cited and celebrated in the cool-star literature. The premise was simple: Rotational velocities of sunlike stars in the few (at the time) well-studied galactic clusters of known age, and the Sun itself, were seen to decline as the square root of time on the main sequence. This correlation famously became known as the Skumanich law.

In parallel, there was a fading of stellar chromospheric activity, as measured by the Ca II HK emissions, as well as a decrease in the lithium abundance, a secondary marker for stellar age. (The primordial light element is slowly burned by low-energy nuclear reactions as material in the stellar envelope is circulated through the hot base of the convective zone, creating a kind of chemonuclear clock.) All of this was contained in a single diagram, reproduced in Fig. 2.6.

The close connection between stellar rotation, age, and activity is fundamental. Cool stars such as the Sun normally begin their lives rotating rapidly, thanks to the swirling Keplerian accretion disks in which they are born. These new stars display intense magnetic effects owing to internal dynamo action, driven by the fast spin. The magnetic activity in turn inspires strong coronal soft x-rays (10^6–10^7 K); far-UV (FUV) (1000—1700 Å) emissions of multiply ionized species such as C IV (few $\times$ 10^5 K), and very bright H I Lyα (2×10^4 K), but also extending down to chromospheric temperatures ($<10^4$ K), for example Ca II HK.

Furthermore, associated with the activity is a hot coronal wind. Far from the star, the ionized plasma in the outflow eventually breaks free of the guiding coronal magnetic fields anchored in the photosphere, and thus can carry away substantial angular momentum, although the mass loss rate itself might seem insignificant (the contemporary solar wind is only about 2×10^{-14} M$_\odot$/year). The persistent angular momentum loss bleeds away the stellar rotation, with a characteristic e-folding timescale of a few hundred million years, at least for young solar-mass stars.

The takeaway message from the Skumanich law is that stellar activity exhibits *negative feedback*: wind braking quenches the dynamo, source of the wind. Thus, the magnetic activity of sunlike dwarfs, as measured by proxies from x-rays to chromospheric Ca II, normally fades over evolutionary time scales.
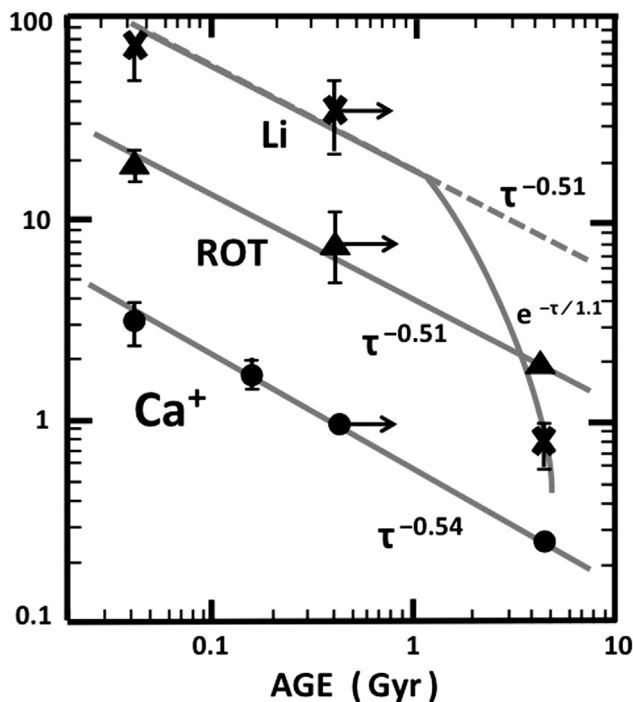
FIGURE 2.6

Rendition of the single figure from the original Skumanich (1972) publication. Points for ages less than 1 billion years (Gyr) come from G stars in young galactic clusters, whereas those at 4.6 Gyr are for the Sun. τ is the stellar age. The *y*-axis is in km/s for the rotational velocities (ROT) and with various scalings in appropriate units for the other two parameters. Note that Li falls anomalously rapidly past age 1 Gyr.

3.2 POST–SKUMANICH LAW INSIGHTS INTO THE ROTATION–AGE–ACTIVITY CONNECTION

After Skumanich's publication, about a decade passed until the early 1980s, when the prolific IUE satellite began to reveal further structure in the rotation–activity diagrams. The most significant advance at the time was when Vilhu and Rucinski (1983) pointed out that at short rotational periods (high spin rates), the 10^5K TZ lines such as Si IV 1393 Å and C IV 1548 Å appeared to saturate, reaching a ceiling (in bolometrically normalized fluxes) reminiscent of the basal limit for Ca II HK mentioned earlier, but now on the high side.

The effect initially was recognized in FUV surveys of short-period, tidally spun-up binary systems, but quickly was seen to apply to fast-rotating single stars as well. Saturation thus appeared to be a universal phenomenon. The high-activity emission ceiling, when expressed as f/f_{bol}, seemed to be roughly independent of effective

temperature and surface gravity. For G-type dwarfs, the C IV normalized flux levels out at about 3×10^{-5}, coronal soft x-rays (0.2—2 keV) near 5×10^{-4}, and chromospheric Mg II at around 3×10^{-4}. The knee between the saturation plateau at fast rotation and the power law decrease in activity with age at the slower rotation rates occurs at a period of a few days for sunlike stars.

Fig. 2.7 illustrates the effect for representative x-ray and Si IV measurements of a sample of ostensibly single, G-type dwarfs. The normalized flux is f/f_{bol}. The saturation behavior in the normalized x-ray fluxes is evident, whereas that in the Si IV emissions is subtler. Aside from the saturation behavior, the figure demonstrates another key aspect of the generalized Skumanich law: namely, the higher-excitation diagnostics (e.g., x-rays) display steeper power laws than the lower-excitation ones (Ca II is about the lowest).

The cause of the saturation behavior is not fully understood, but one can imagine that an overproductive dynamo might clog the stellar surface with strong fields, suppressing convection, and thereby partially insulating the flux ropes from the granular buffeting that normally would cause heating higher up.
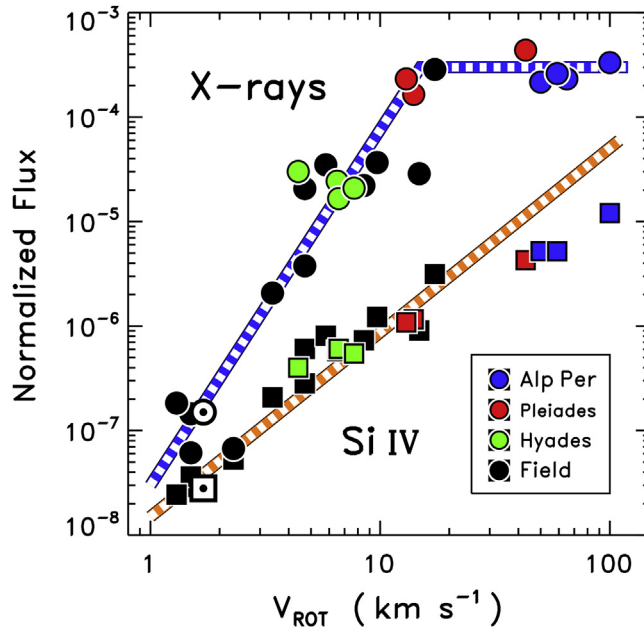

FIGURE 2.7

Saturation of x-rays and Si IV at high rotation rates for single solar-type stars. The *y*-axis is f/f_{bol}. Cluster stars are shaded according to the legend. Solar values are marked by open symbols with dots. The more active field stars are members of the young Ursa Major Stream. Note that the high-energy x-rays rise steeply and then abruptly level off, whereas the cooler Si IV emissions rise more slowly and fall away less dramatically from the power-law behavior extrapolated from low rotational velocities. *Alp Per,* Alpha Persei.

Rossby Number. The Skumanich relation shows a spread among stars of different spectral types on either side of the tight trend displayed by G dwarfs (as illustrated in the original Skumanich article). In the early 1980s, R. Noyes and colleagues (Noyes et al. 1984)showed that the apparent spectral-type dispersion could be collapsed into a single, tighter relationship by introducing a new independent variable called the Rossby number, $Ro = P_{rot}/\tau_{conv}$, where P_{rot} is the rotational period and τ_{conv} is a convective overturning timescale (estimated from stellar structure models).

The Rossby number itself appears in theoretical descriptions of the dynamo mechanism, so it is unsurprising that it would emerge as a consolidating factor in the rotation−activity diagrams. The generally accepted solar value is around $Ro \approx 2$ (which implies that the overturning timescale is about half a month).

Spin Ages: Gyrochronology. The Skumanich law says that single late-type stars spin down systematically over their lifetimes. Thus, the rotation period of a star should be a proxy for its age. Stellar ages are notoriously difficult to determine, especially for low-mass stars that change little in outward appearance over long timescales (billions of years at solar mass); rotation is the main exception (and Li abundance is a secondary one). The association between age and spin was coined gyrochronology by S. Barnes (2003).

If the pure Skumanich law were operating, dwarf stars of similar type would spin down together synchronously over time and all would be well with gyrochronology. However, early on, it was recognized that G dwarfs, as an example, were not all born with the same rotation period. Instead, the youngest open clusters showed a spread in rotational periods among the presumably coeval cohort of G stars. Curiously, as noted by Stauffer and Hartmann (1987), the broad distribution of initial spin periods at early ages (say, in the Alpha Persei cluster, 50 million years [Myr] old), apparently narrows by later times (e.g., the Pleiades, 100 Myr) and then funnels to a very tight band at the age of the Hyades cluster (600 Myr). This behavior is illustrated schematically in Fig. 2.8. The spin funneling effect undoubtedly is because more active, fast rotators have larger angular momentum loss and thus spin down more rapidly. Meanwhile, slower rotators are less active and thus experience reduced magnetic braking.

The rotational convergence effect was exploited by Ayres (1997) as part of an effort to estimate the Sun's activity levels at the time planetary atmospheres in our solar system were recovering from the so-called Late Heavy Bombardment (LHB). This was an epoch when planetary surfaces were remodeled by incessant planetesimal impacts over a relatively short period, perhaps a million years or so, probably about 600−800 Myr after the solar system formed. It had been speculated at the time that the Sun's hyperactivity during that youthful period, particularly the corrosive effects of ionizing radiation and magnetized coronal wind, might have stripped away the early atmosphere of Mars. The atmospheric escape would have rendered the planet, initially in the habitable zone with perhaps a shallow northern sea, not so hospitable later on. Thanks to the LHB episode in our Solar System, which reset the clock for planetary atmospheres at the equivalent of about Hyades age (around 600 Myr), the rotational convergence effect has an important practical
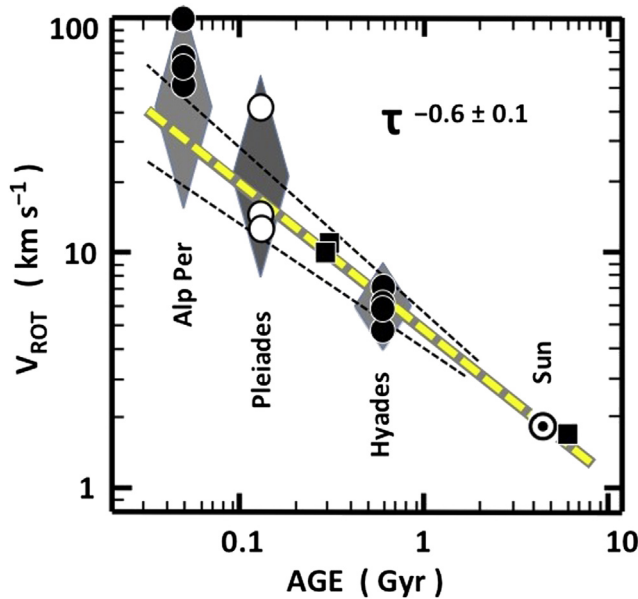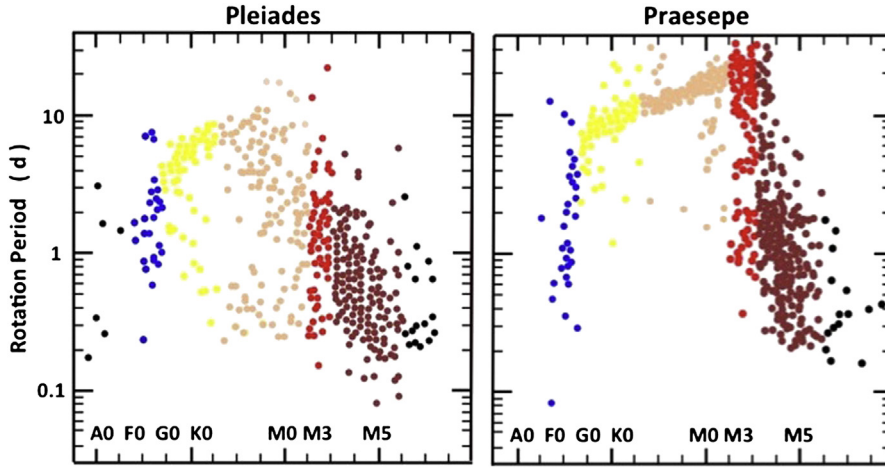
FIGURE 2.8

Rotational convergence effect, reproducing general $t^{-\frac{1}{2}}$ trend of original Skumanich law but emphasizing spread of rotational velocities in youngest clusters (depicted by shaded diamonds). Broad distribution at early times has narrowed by Hyades age (≈ 600 Myr). Symbols represent selected sunlike stars from Fig. 2.7. *Alp Per*, Alpha Persei; *Gyr*, billion years.

consequence: We now think we know almost exactly what the high-energy irradiances from the young Sun were like in those days (according to the converged Hyades example), which then serve as input into sophisticated atmospheric chemical evolution models for the rocky worlds of the inner solar system.

Kepler Studies of Young and Intermediate-Age Open Clusters*.* More recently, the study of rotational properties of open cluster stars has received a welcome boost from the planet-hunting Kepler satellite. This was especially so during its extended K2 mission, when the satellite focused on a $10° \times 10°$ patch of sky near the ecliptic for about a month at a time and then moved on to a new pointing, ultimately covering dozens of such fields. Kepler's extremely precise optical photometry is well-suited to assess rotation rates of late-type stars via starspot modulations, particularly in young clusters where spin periods are around 10 days or less, so that several rotational cycles could be captured for each target to solidify the statistics.

Stauffer et al. (2016) and Rebull et al. (2017) have described Kepler measurements of hundreds of cluster members covering F—M spectral types in the young Pleiades (≈ 100 Myr) and intermediate-age Praesepe (≈ 800 Myr). The left-hand

FIGURE 2.9

Rotation period distribution of ≈100-Myr Pleiades cluster (left) compared with ≈800-Myr Praesepe (right).

Adapted from Rebull, L.M., Stauffer, J.R., Hillenbrand, L.A., et al., 2017, Astrophys. J. ***839***, 92.

panel of Fig. 2.9 depicts rotational period distributions of Pleiades dwarfs as a function of spectral type. The sample is divided into several mass bins (colors), with fully convective stars to the right and sunlike types to the left. The diagram is filled in the middle and has sloping wings on either side (early-F stars and late-M's). The G and K dwarfs show a spread in rotational periods, from very fast to moderately fast, whereas the F and M stars have tighter distributions shaded toward shorter periods.

The right-hand panel depicts the rotational period distribution in the older Praesepe cluster. Now, the previous curtain of points has lifted up: the G and K dwarfs have converged into a narrower distribution of moderate rotation periods. Meanwhile, the flanking F and M wings have risen somewhat but still exhibit shorter periods than the G/K dwarfs, suggesting that spin-down times for both extreme types are longer than for more mainstream sunlike stars.

This demonstrates that the rotational funneling effect works for a wide range of spectral classes, except those at the extremes: one side (early-F) at the edge of convection and the other (late-M) with convection fully engaged.

3.3 THEORY BEHIND THE SKUMANICH LAW

One implication of the Skumanich law is that the chromospheric Ca II HK luminosity must be linearly related to the rotation of the star because both quantities decay at the same rate. Furthermore, because the HK intensity is known to depend on the surface magnetic field (Frazier, 1970; Skumanich et al., 1975), the latter must be linearly related to the angular velocity as well. This is important because the spin braking mechanisms described below depend on the stellar surface field.

In the early 1960s, Schatzman (1962) introduced the concept of magnetic wind braking, although focusing on the convective phase of pre-Main sequence evolution. Later, Weber and Davis (1967) outlined basic principles of wind angular momentum loss for the contemporary Sun, assuming a steady outflow analogous to the Parker (1966) coronal wind solutions published the previous year. The authors' fundamental result was encapsulated in a deceptively simple torque equation, $dJ_\odot/dt = \frac{2}{3}\Omega_\odot r_a^2 dM_\odot/dt$, where $J_\odot$ is the solar angular momentum (whose time derivative represents a torque); $\Omega_\odot$ is the angular rotation rate; r_a is the Alfvén radius, where the wind flow breaks away from the extended corotating coronal magnetosphere (which, in turn, depends on the global field); and the final term is the mass loss rate. The Alfvén radius can be large, dozens of $R_\odot$, and enters the torque equation squared, so its influence is greatly magnified. Thus, an almost negligible coronal wind mass loss rate can significantly affect the solar rotation over evolutionary timescales.

Once the torque has been characterized as a function of time, the rotational evolution of a star can be determined by integrating the angular momentum from some initial condition, and then dividing the instantaneous $J_*(t)$ by the stellar moment of inertia $I_*(t)$ (which could include the changes in the stellar structure over time, albeit small and slow) to obtain $\Omega_*(t)$. The choice of the initial condition is complicated by a number of effects, especially the possibility that magnetic fields could lock the stellar rotation onto the inner Keplerian accretion disk, thus altering the spin evolution at very early times. Another more fascinating but less well-documented influence could be engulfment of hot Jupiters in-spiraling through the disk owing to tidal migration, which could boost the angular momentum of the host star, perhaps episodically.

Furthermore, the time evolution of the mass-loss rate is poorly known, mainly because the very hot and tenuous stellar winds cannot be detected directly by conventional means. So far, only indirect methods have been available, such as assessing the impact of a wind as it blows a bubble in the local interstellar medium (Wood and Linsky, 1998; Wood et al., 2002). Because of these observational uncertainties, significant effort has focused on parameterizing the torque equation in a few essential theory-motivated properties, usually as distilled from numerical simulations of prototype magnetic field configurations in the stellar corona and what types of self-consistent mass flows these might support. The crucial Alfvén radius depends on the radial falloff of the strength of the magnetic field in the outer corona, as extrapolated from a surface boundary value B_*. The tension forces in the outer magnetosphere are balanced against the dynamical pressure of the flow, which depends on speed and density, in turn conflated with the mass loss rate. Some field configurations might support a larger mass loss rate but a smaller breakaway radius, so that the torque actually could be reduced, and vice versa.

A further important consideration is the saturation of activity that can occur at short spin periods and what that might imply for the surface organization of the strong magnetic fields. Finally, there is the related question of what proportion of the coronal field is open to interplanetary space, and thus can support a mass flux

and associated wind braking, versus the volume of closed field, which would have a more passive role in the angular momentum loss (but contribute directly to the high-energy luminosity of the star).

An example of a modern version of the torque equation for a global dipole field configuration, from a study published by S. Matt et al. (2012) is:

$$\tau_{\mathrm{w}} = K_1^2 B_*^{4m} \dot{M}_{\mathrm{w}}^{1-2m} R_*^{4m+2} \frac{\Omega_*}{\left(K_2^2\, v_{\mathrm{esc}}^2 + \Omega_*^2 R_*^2\right)^m}$$

where τ_w is the wind torque; K_1, K_2, and m are dimensionless constants derived from numerical simulations (with fitted values of 1.30, 0.051, and 0.22, respectively, for this particular case); B_* is the surface magnetic field strength; $\dot{M}_{\mathrm{w}}$ is the wind mass flux; R_* is the stellar radius; Ω_* is the equivalent solid-body rotation rate ($2\pi/P_{\mathrm{rot}}$); and v_{esc} is the surface escape speed. Note that the torque law depends linearly on the angular rotational velocity at small Ω_*, but it has a more complex and weaker dependence at higher Ω_*, as might be anticipated by the saturation effects noted earlier.

In the final analysis, the Skumanich law provides an observational framework within which such numerically calibrated semianalytical treatments must operate, so there is reason to hope that a self-consistent picture of the magnetic braking process can be pieced together someday.

4. STELLAR ACTIVITY CYCLES

For our middle-aged Sun, magnetic activity varies on a stunning array of timescales. On the longer side, it ranges from the iconic 11-year ebb and flow of sunspots (the Schwabe cycle, which, in fact, is a 22-year Hale cycle when polarity reversals of the global field are taken into account), up to a century for slower modulations (e.g., the Gleissberg cycle) recognized from studies of isotope decay in tree rings and ice cores, with suggestions of even more extended variations up to a millennium or more. On the shorter side, changes are seen as active regions emerge and decay (months), on rotational timescales (a month) caused by asymmetric distributions of activity on the solar surface, all the way down to transient, intense flare outbursts (seconds to hours). Of all these variations, the 11-year sunspot cycle is perhaps the most striking.

In fact, many late-type dwarfs exhibit decadal activity cycles that resemble the solar counterpart. Most stellar cycle periods are from the long-term Ca II HK monitoring effort originally started by O. C. Wilson in the 1960s and continued in various guises to the present day. The HK emission itself is a useful proxy for stellar activity because it arises mainly in spatially extensive chromospheric plage areas surrounding starspots (Fig. 2.1).

The HK programs normally record the S-index, a ratio of the combined fluxes of the Ca II emission cores in narrow ≈ 1 Å triangular windows, divided by a reference continuum flux, in a pair of flanking, broader wavelength bands out in the line wings. The HK differential measurement is insensitive to seeing and transparency

fluctuations, but a color-dependent correction must be made to convert the index to an absolute surface flux.

There have been many accounts of these HK programs (Wilson et al., 1981; Duncan et al., 1991; Baliunas et al., 1995; Radick et al., 1998; Lockwood et al., 2007), which can be summarized as follows:

1. Sunlike decadal cycles are common among low-activity dwarf stars.
2. Some stars show evidence of multiple cycles, typically two: one with a few-year period and the other a decade or more.
3. Examples of Maunder Minimum behavior (referring to a 7-decade span in the 17th century when sunspots were rarely seen) are found in a modest fraction (perhaps 30%) of the low-activity objects. However, some of these are subgiant stars, for which post-Main-sequence spindown likely has been severe.
4. Active dwarfs show less obvious evidence for cycles. If cycles are present, they typically are short. Also, the HK light curves of active stars are noisy owing to short-term rotational modulations.

Almost all of our empirical knowledge of starspot cycles has come from these long-term HK programs. However, Ca II is a low-contrast diagnostic because its formation is less closely tied to chromospheric conditions than, say, optically thicker Mg II hk. The advantage of Ca II, of course, is easy access from the ground.

The highest-contrast, practical diagnostic for recording activity cycles is soft x-ray (0.2−2 keV) emission. Hard x-rays or γ-rays are too faint for routine detection, whereas extreme UV features such as He II 304 Å are blocked by interstellar extinction, except in the very nearest stars.

Fig. 2.10 illustrates soft x-ray time series for the Sun, Alpha Centauri (α Cen) A (G2 V) and B (K1 V), and another nearby star, mid-F subgiant Procyon (α Canis Minoris; F5 IV-V). Post-2005 observations (dots) are from Chandra's High-Resolution Camera. Asterisks (2003−11) are from XMM-Newton (α Cen B only: A was difficult to record because of technical issues). A single pair of AB points in 2000 is from Chandra's Low-Energy Transmission Grating Spectrometer (LETGS). Multiple Procyon values in the same epoch also are from LETGS. Pre-2000 AB points are from the ROSAT High-Resolution Imager. Sun-as-a-star x-ray fluxes were taken from the Flare Irradiance Spectral Model (FISM), which uses an automated emission-measure approach to regularize solar broad-band energy spectra aggregated from several sources.

Curiously, the smallest star (α Cen B) has the highest activity level, in L_X/L_{bol}, whereas its visually brighter companion, A, has the lowest. The Sun and Procyon are in the middle. B shows a clear x-ray cycle with a period of about 8 years, shorter than the Sun's iconic 11 years. The series for Procyon so far has been trending slightly downward, but possibly just reflecting a slow decline in instrumental sensitivity. The situation for solar-twin α Cen A is more ambiguous: a suggested maximum in the mid-1990s, a possible new peak in the mid-2010s, but a flat activity period 2005−10. If the two maxima represent a true cycle, the period is about 19 years. On the other hand, the low-activity lull might be an analog of the extended
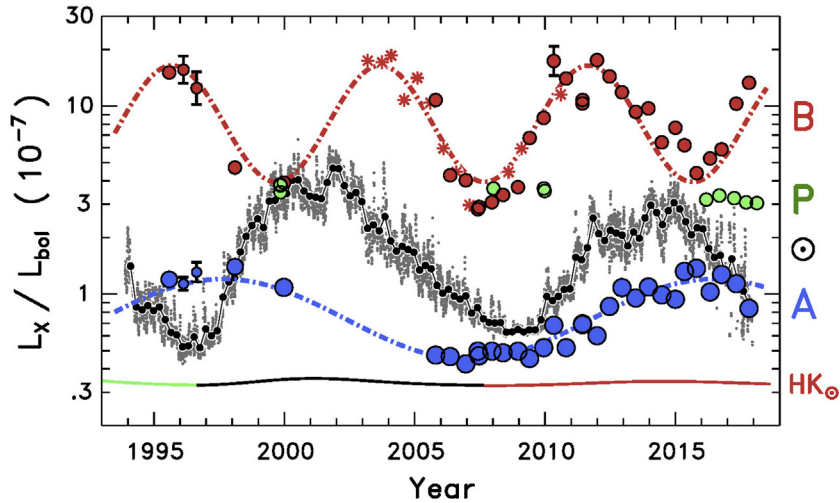
FIGURE 2.10

X-ray cycles of the Sun ($\odot$), Alpha Centauri (A/B), and Procyon (P). Ordinate is the bolometrically normalized soft x-ray flux (0.2–2 keV), which allows a fairer comparison among these different objects (mainly in terms of stellar radius). Larger dots in the solar curve are 81-day means (three rotations) of daily averages (lighter points); excursions of the daily values illustrate amplitudes of rotational modulations. Solid curves in lower part of the diagram are fitted trends of the solar Ca II HK S-index, as reported by Egeland et al. (2017).

solar minimum preceding the rise of contemporary Cycle 24 (compare 2007–10 with previous minimum, 1996–97).

A crucial takeaway from the diagram is that the x-ray cycle amplitudes are enormous, factors of several to 10, whereas Ca II cycle modulations (solid curves in lower part of figure) are nearly flat lines on the logarithmic scale (only about 15% in amplitude). Despite the high sensitivity to cycles, x-ray monitoring programs are challenging because observing time on heavily oversubscribed facilities like Chandra is difficult to obtain.

As in the previous sections, the goal here is to describe an aspect of stellar behavior that might be relevant to understanding the more singular case of the Sun.

The best example, aside from the summary points made earlier, is the suggestion of systematic structure in a diagram comparing cycle durations with rotation periods. The spin periods are significant because differential rotation has an important role in the starspot-spawning dynamo, and the latitudinal flows themselves are a by-product of an interaction between solid-body rotation and convection.

In the late-1990s, Saar and Brandenburg (and later Böhm-Vitense (2007)), pointed out that the P_{cyc} versus P_{rot} diagram seemed to show distinct tracks. Saar and Brandenburg (1999) called these the active branch, mostly faster rotators

($P_{rot} < 20$ d), following a steep dependence of P_{cyc} versus P_{rot}; and an inactive branch, mostly slower rotators ($P_{rot} > 20$ d), showing a shallower slope of P_{cyc} versus P_{rot}. Some stars displayed double periods and thus could sit on both branches.

A schematic rendition of the Böhm-Vitense (2007) version of the diagram is illustrated in Fig. 2.11. The remarkable aspect is that the cycle and spin timescales differ by roughly two orders of magnitude, yet enough of a connection exists to impose some apparent order. As noted by Böhm-Vitense, the number of rotational cycles per starspot period appears to be constant on the two branches, but it differs by a factor of about six between them. The Sun sits in the middle of the diagram, not especially close to either branch. This raised the possibility that the Sun is unique in some important respect that would cause it to occupy its isolated position.

The two circled points refer to the α Cen stars (based on their apparent X-ray cycles). Curiously, coronally weak α Cen A falls on the active branch whereas its x-ray brighter companion sits squarely in the middle of the inactive branch (although in a region populated mainly by later-type dwarfs, so perhaps it is unsurprising that α Cen B is found there).
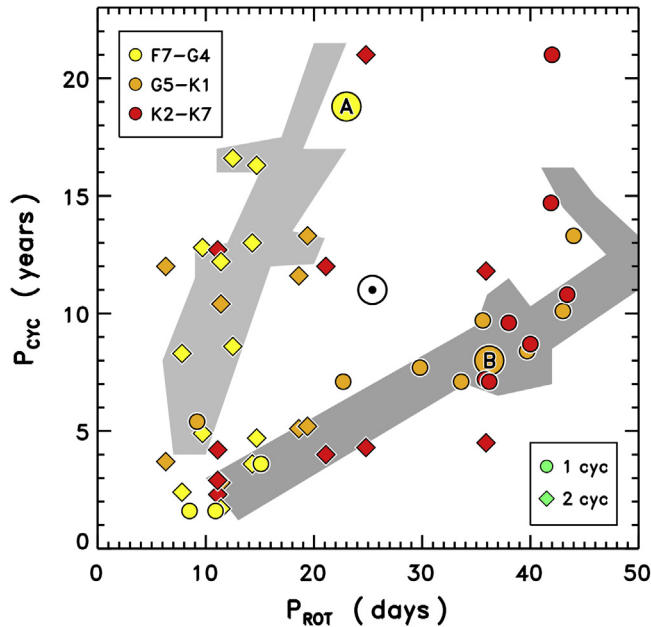

FIGURE 2.11

Spot cycle duration (P_{cyc}) versus rotational period (P_{rot}). Circled A and B symbols refer to Alpha Centauri AB. Shaded areas are the active (left) and inactive (right) branches from the original publication. Symbols are values aggregated from several additional sources.

Adapted from Böhm-Vitense, E., 2007. Astrophys. J. ***657***, 486.

A more recent reevaluation of the older measurements, including newer observations and additional objects, by R. Egeland in his doctoral thesis (Egeland 2017) suggests that the previously coherent branches dissolve into fuzzier blobs of points, now making the Sun less of an outlier.

The filling-in of the diagram is disappointing in the sense that the previous structure offered a possible avenue to a theoretical description. In fact, the superficial lack of correlation between cycle duration and rotation period for many of the stars seems to suggest that there is a hidden parameter yet to be identified that might unify the behavior across the range of stellar types, something like what the Rossby description did to collapse the color dependence of the broader rotation—activity connection. Alternatively, the dynamo might be a low-Q oscillator such that a coherent period can be maintained only for a few dozen cycles, after which a new modulation engages, longer or shorter than before. In that situation, our view of the solar cycle could be biased by the limited historical time frame, and thus our perception that it is an entirely regular phenomenon might be unfounded.

Unfortunately, the study of long-term stellar activity cycles benefits little from better instrumentation, or a larger telescope, but rather *time* itself is the adversary. Thankfully, Olin Wilson showed keen insight in starting the Mount Wilson HK program a half-century ago. Although crude by modern standards, the historical measurements nevertheless were scalable to future monitoring efforts using the flux ratio strategy he devised, achieving the long-term continuity that is at the heart of the hunt for stellar cycles. It is sobering to realize that alternative programs, exploiting different observational techniques or following vastly expanded stellar samples, started today would bear fruit only decades from now.

REFERENCES

Anderson, L.S., Athay, R.G., 1989. Astrophys. J. 346, 1010.
Ayres, T.R., 1975. Astrophys. J. 201, 799.
Ayres, T.R., 1979. Astrophys. J. 228, 509.
Ayres, T.R., 1997. JGR (Planets) 102, 1641.
Ayres, T.R., Linsky, J.L., 1975. Astrophys. J. 200, 660.
Baliunas, S.L., Donahue, R.A., Soon, W.H., et al., 1995. Astrophys. J. 438, 269.
Barnes, S.A., 2003. Astrophys. J. 586, 464.
Böhm-Vitense, E., 2007. Astrophys. J. 657, 486.
Burgess, A., Tully, J.A., 1992. Astron. Astrophys 254, 436.
Chianti Atomic Database. http://www.chiantidatabase.org.
Collier Cameron, A., Duncan, D.K., Ehrenfreund, P., et al., 1990. MNRAS 247, 415.
Duncan, D.K., Vaughan, A.H., Wilson, O.C., et al., 1991. Astrophys. J. Suppl. 76, 383.
Egeland, R., 2017. (Ph.D. thesis). Montana State University, Bozeman, Montana, USA.
Egeland, R., Soon, W., Baliunas, S., et al., 2017. Astrophys. J. 835, 25.
FISM database. http://www.lasp.colorado.edu/lisird/data/fism/.
Frazier, E.N., 1970. Sol. Phys. 14, 89.
Hoyle, F., Wilson, O.C., 1958. Astrophys. J. 128, 604.

Huenemoerder, D.P., Ramsey, L.W., Buzasi, D.L., et al., 1993. Astrophys. J. 404, 316.

Linsky, J.L., 1999. Astrophys. J. 525, 776.

Linsky, J.L., Ayres, T.R., 1978. Astrophys. J. 220, 619.

Lockwood, G.W., Skiff, B.A., Henry, G.W., et al., 2007. Astrophys. J. Suppl. 171, 260.

Maltby, P., Avrett, E.H., Carlsson, M., et al., 1986. Astrophys. J. 306, 284.

Matt, S.P., MacGregor, K.B., Pinsonneault, M.H., et al., 2012. Astrophys. J. 754, L26.

McMurry, A.D., 1999. MNRAS 302, 37.

Noyes, R.W., Hartmann, L.W., Baliunas, S.L., et al., 1984. Astrophys. J. 279, 763.

Parker, E.N., 1966. Astrophys. J. 143, 32.

Radick, R.R., Lockwood, G.W., Skiff, B.A., et al., 1998. Astrophys. J. 118, 239.

Rebull, L.M., Stauffer, J.R., Hillenbrand, L.A., et al., 2017. Astrophys. J. 839, 92.

Saar, S.H., Brandenburg, A., 1999. Astrophys. J. 524, 295.

Schatzman, E., 1962. Ann. Astrophys. 25, 18.

Skumanich, A., 1972. Astrophys. J. 171, 565.

Skumanich, A., Smyth, C., Frazier, E.N., 1975. Astrophys. J. 200, 747.

Stauffer, J.R., Hartmann, L.W., 1987. Astrophys. J. 318, 337.

Stauffer, J., Rebull, L., Bouvier, J., et al., 2016. Astron. J. 152, 115.

Thomas, R.N., Athay, R.G., 1961. Physics of the Solar Chromosphere. Interscience, New York (Chapter 5).

Vernazza, J.E., Avrett, E.H., Loeser, R., 1981. Astrophys. J. Suppl. 45, 635.

Vilhu, O., Rucinski, S.M., 1983. Astron. Astrophys. 127, 5.

Weber, E.J., Davis Jr., L., 1967. Astrophys. J. 148, 217.

Wilson, O.C., Bappu, V.M.K., 1957. Astrophys. J. 125, 661.

Wilson, O., Vaughan, A., Kraft, R., et al., 1981. Sky Telesc. 62, 312.

Wood, B.E., Linsky, J.L., 1998. Astrophys. J. 492, 788.

Wood, B.E., Müller, H.-R., Zank, G.P., et al., 2002. Astrophys. J. 574, 412.